Journal of
Synchrotron Radiation

ISSN 0909-0495

Received 5 May 2012
Accepted 30 July 2012

Coupling transmission electron microscopy with synchrotron radiation X-ray fluorescence microscopy to image vascular copper

Zhenyu Qin,[a,b]*‡ Barry Lai,[c]‡ Julio Landero[d] and Joseph A. Caruso[d]

[a]Division of Vascular Surgery, Department of Surgery, University of Texas Health Science Center at San Antonio, San Antonio, TX 78229, USA, [b]Division of Cardiovascular Disease, Department of Medicine, University of Cincinnati, Cincinnati, OH 45267, USA, [c]X-ray Science Division, Argonne National Laboratory, Argonne, IL 60439, USA, and [d]Department of Chemistry, University of Cincinnati, Cincinnati, OH 45267, USA. E-mail: qinz@uthscsa.edu

Recently, using synchrotron radiation X-ray fluorescence microscopy (SRXRF), the copper accumulation in rat aortic elastin and copper topography in human THP-1 cell monolayer have been described. However, it is necessary to locate more accurately cellular copper in the vascular cells and tissues. In the current study, SRXRF coupling with transmission electron microscopy (TEM) was used to image copper in sections of human THP-1 cells and mouse aorta. The results showed that sections of 1 μm thickness are required for SRXRF producing a correlative image with TEM between copper topography and cellular ultrastructure. As compared with SRXRF alone, coupling TEM with SRXRF can clearly identify the location of copper in the nucleus and nucleolus in non-dividing THP-1 cell sections, and can differentiate the copper location at elastic laminae from collagen in mouse aortic sections. Thus, these results revealed new information about the copper topography in vascular cells and tissues and highlighted the potential of TEM-SRXRF to investigate the role of copper in macrophage and aortic homeostasis.

Keywords: transmission electron microscopy; synchrotron radiation X-ray fluorescence microscopy; copper; imaging; macrophage; aorta.

1. Introduction

Copper is an essential biometal in humans. However, progress in investigating the role of copper in vascular homeostasis lags behind that of several other biometals, including calcium, magnesium, iron and zinc, partly because copper concentrations in cells and tissues are relatively lower. In general, only histochemistry methods can detect copper in some liver and brain tissues from patients with Wilson disease (Szerdahelyi & Kasa, 1984), in which the copper concentrations are significantly higher than normal. Pilloni *et al.* (1998) found that the copper detection sensitivity is low in three common histochemical methods (rhodanine, orcein and Timm's silver stains) and has limited value in diagnosing human Wilson's disease. The same study also showed a significant variation in the copper concentrations in the liver needle biopsies detected by atomic absorption spectrometry (air-acetylene flame), between 36 and 3154 μg g^{-1} dry tissue (Pilloni *et al.*, 1998). Because a liver needle biopsy does not always take tissue specimens from the same location, this significant variability might partly be due to the inhomogeneous distribution of copper within the liver, which needs to be confirmed in future independent cohorts of patients with ATP7B mutations. Note that the mean liver copper concentrations may be 983 μg g^{-1} in a patient with early Wilson disease and 493 μg g^{-1} in a patient with late Wilson disease (Lellingsen *et al.*, 2007), while the liver copper concentration can reach 1370 μg g^{-1} dry weight in the liver of an untreated patient with Wilson's disease (Lellingsen *et al.*, 2007). In addition to histochemical methods, Abs *et al.* (1989) developed a colorimetric assay to detect copper in the serum using compounds such as pyridylazo and thiazolylazo as colour reagents. This method has been applied to study the alteration in serum copper in patients with various diseases, such as traumatic brain injury (Dash *et al.*, 2010), Down syndrome (Meguid *et al.*, 2010) and acute stroke (Altamura *et al.*, 2009). The major limitation of histochemistry methods and the colorimetric assay is that they can only detect copper under certain limited conditions, whereas several analytical chemical techniques can overcome these limitations. For example, since being introduced in 1955 (L'vov, 2005), atomic absorption spectrometry has become the most widely applied technique for detecting copper in biolo-

‡ These authors contributed equally to the publication.

gical samples, such as plasma (Canatan *et al.*, 2004), serum (Taneja & Mandal, 2007) and urine (Taneja & Mandal, 2007). In the early 1980s, inductively coupled plasma mass spectrometry (ICP-MS) was introduced (Beauchemin, 2002) and presented multi-element capability in biological applications. However, neither of these techniques was designed to image biometals at the cellular scale. Recently, Becker *et al.* (2010) proposed coupling a laser microdissection apparatus with an ICP-MS, also called LMD-ICP-MS, to study the metal concentration in a single cell.

The physical property of each element producing characteristic X-ray emission lays the foundation for developing another independent technique for studying the metal topography in biological samples (Qin, Caruso *et al.*, 2011). As a result, energy-dispersive X-ray emission spectroscopy (EDX) has been used to detect biological elements for half a century (Irons *et al.*, 1976). Electrons, protons and X-rays excitation can be used to generate characteristic X-ray emissions. However, only X-rays as a beam source can offer high sensitivity and a low radiation dose simultaneously (Twining *et al.*, 2003). Although synchrotron radiation X-ray fluorescence microscopy (SRXRF) is derived from EDX, SRXRF uses synchrotron radiation as an X-ray source (Jones *et al.*, 1988). It can significantly reduce scattering from the specimen (Chevallier *et al.*, 1996) and offers significantly higher brightness than traditional laboratory sources. In addition, with the introduction of the Fresnel zone plate, incident X-rays can be focused with higher efficiency and limited background generated by unwanted diffraction (Yun *et al.*, 1999). Therefore, these earlier studies indicate that SRXRF can open a new door to investigate biometals in vascular samples.

In order to accurately locate elemental topography, the following two techniques have been coupled with SRXRF to reveal the location of copper in cells and tissues.

(i) Light microscopy can generate an image that is comparable with the image generated by SRXRF. For example, Finney *et al.* (2007) revealed significant copper translocation in human microvascular endothelial cells in response to angiogenic stimulations, whereas the cell shape detected by light microscopy helps to differentiate the intracellular copper from extracellular copper. Similarly, Ralle *et al.* (2010) described copper topography in extracellular deposits and inflammatory cells in the liver of ATP7B-deficient mice, whereas hematoxylin and eosin staining detected by light microscopy helps to differentiate intracellular from extracellular spaces. In our recent studies we detected the copper accumulation in rat aortic elastin by comparing hematoxylin and eosin staining and Verhoeff's staining (Qin, Toursarkissian *et al.*, 2011), and estimated the copper topography in the whole THP-1 cell monolayer (Kim *et al.*, 2012).

(ii) Fluorescence microscopy is used to identify the cellular structure using organelle-specific stain or antibodies. Glesne *et al.* (2006) used DAPI (10 μg ml^{-1}) to stain the nuclei in HL-60 cells and then mounted the cells on electron microscopy grids for elemental detection. McRae *et al.* (2006) investigated cellular metal localization in mitochondria and the *cis*-Golgi apparatus of mouse fibroblast cells using antibodies conjugated to colloidal gold particles. However, although transmission electron microscopy (TEM) has been coupled with EDX to study the copper topography in biological samples, particularly the hepatic tissues derived from patients with Wilson's disease (Jonas *et al.*, 2001) and its associated animal model (Gross *et al.*, 1989), few correlative studies had been performed to assess whether TEM can also provide complementary information to localize copper in vascular cells and tissues when coupling with SRXRF; thus, this will be investigated in this study.

2. Methods

2.1. Cells and animals

The human THP-1 cell line was obtained from the American Type Culture Collection (Rockville, MD, USA) and maintained in culture using RPMI 1640 medium (Hyclone, Logan, UT, USA) in the presence of 10% fetal bovine serum, penicillin (100 units ml^{-1}) and streptomycin (100 μg ml^{-1}). Cultures were maintained in 5% CO_2 tissue culture incubators maintained at 310 K until ready for use. C57BL/J mouse (Jackson Laboratory, Bar Harbor, MN, USA) was fed with normal chew diet with the normal dietary requirements of copper. The experimental protocol was approved by the IACUC at the University of Cincinnati.

2.2. Trace-metal contamination precautions

All chemicals used were analytical grade or of high purity. Sampling procedures were performed in a laminar-flow clean-air bench. Milli-Q water (18 MΩ) was used for buffer preparation. Only clear and new plastic tips, microcentrifuge tubes and sample containers were used.

2.3. Preparation of human THP-1 cells

THP-1 cells (2×10^6) were treated with 50 μm $CuSO_4$ overnight, briefly washed with phosphate-buffered saline (PBS) and centrifuged at 1000 RPM for 10 min. After that, a cell pellet was collected and fixed in 2.5% glutaraldehyde (EMS, Hatfield, PA, USA) in PBS, pH 7.4, for 15 min. Following treatment with 1% osmium tetroxide (EMS) in PBS for 30 min at room temperature, the cell pellets were dehydrated in series of graded ethanol (Sigma, ACS reagent) to 100%. Pellets were then incubated sequentially with 3:1 and 1:1 of ethanol:resin (EMS), 30 min each, followed with pure resin for 24 h, all at 253 K. Finally, pellets were polymerized at 323 K for 24 h, until the block was totally solidified for further experiments.

2.4. Preparation of mouse aorta

After sacrifice, segments of thoracic aorta were prepared and immediately fixed in 2.5% glutaraldehyde in PBS overnight, pH 7.4, at 277 K. After washing in PBS, the samples were treated with 1% osmium tetroxide in PBS for 30 min at room temperature. The samples were then rinsed in PBS twice and dehydrated through a series of ethanol concentrations

graded to 100%. Samples were incubated overnight on a shaker in a 1:1 solution of resin:ethanol at room temperature. Afterwards the sample was embedded in fresh 100% resin overnight at 333 K.

2.5. TEM

Sections of resin-embedded cells and tissues were cut on an ultramicrotome. The sections were first stained with toluidine blue to examine the integrity of the samples. Serial sections were then mounted on electron microscope grids. We chose a carbon-formvar-coated gold Gilder finder grid (200 mesh, pitch 125 µm, hole 106 µm and bar 25–12 µm; EMS) in which the grid is divided into nine thin bar areas, which are identified by alphabetical letters located in the centre of the grid. The sections on gold grids were observed using a Zeiss transmission electron microscope. The representative biological structures on the grid were located based on its association with an alphabetical letter so that the same area could be found by an optical microscope (Leica DMXRE) for further SRXRF study.

2.6. SRXRF

Copper topography was analyzed by SRXRF at the 2-ID-D beamline of the Advanced Photon Source at Argonne National Laboratory (Argonne, IL, USA). The cell or tissue sections on the gold grids were mounted on a kinematic specimen holder appropriate for both optical and SRXRF microscopes. Under the optical microscope the representative biological structures on the gold grid were located relative to the reference points on a grid using encoder coordinates from the *x*/*y* stages. The coordinates were then used to locate the same biological structures as the target area under SRXRF microscope. A monochromatic X-ray beam generated from a synchrotron radiation source was focused to a spot size of 0.3 µm × 0.2 µm (horizontal × vertical) on the target area using a Fresnel zone plate. An incident energy of 10 keV was chosen for copper excitation. The tissue section was subsequently raster-scanned through the beam at 298 K under a He atmosphere. The pixel step size was set to 0.5 µm with a dwell time of 4 s, and the copper X-ray fluorescence spectrum was recorded using an energy-dispersive silicon drift detector (SII NanoTechnology, Northridge, CA, USA). Spectral fitting was performed using a modified Gaussian mathematical model to determine the characteristic copper *Kα* fluorescence peak signal, and using an adapted version of the SNIP algorithm to estimate the background signal (van Espen, 2002). Fluorescence signal strength of copper is the characteristic fluorescence peak signal corrected by the background signal. The copper area density (pmol cm^{-2}) was calculated using MAPS software (Vogt, 2003) by comparing the fluorescence signal strength from a target area with a calibration curve generated from the thin-film standards SRM 1832 (National Institute of Standards and Technology, Gaithersburg, MD, USA). Fig. 1 illustrates the basic principle of SRXRF-TEM.

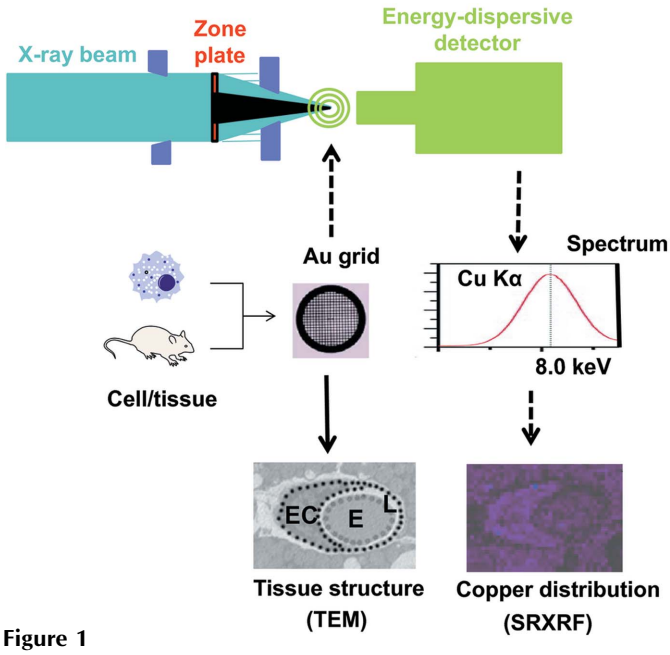

Figure 1
Principle of using TEM-SRXRF to detect copper location in cells and tissues. The first step is to prepare the semithin sections of cells and tissues using a glutaraldehyde-fixed and resin-embedded approach, and to load the section onto a gold (Au) grid. TEM (solid bold line) and SRXRF (dashed bold lines) are then used to detect the cell or tissue ultrastructure and copper topography, respectively. For SRXRF, a monochromatic X-ray beam (blue) generated from a synchrotron radiation source was focused to a submicrometre spot on the sample section using a Fresnel zone plate (red). An energy-dispersive silicon drift detector (green) was used to collect the copper X-ray fluorescence spectrum. *MAPS* software was used to analyze the fluorescence data and to generate a copper image. The final SRXRF image (bottom right) represents copper topography in an aortic adventitial capillary vessel of a C57B/l mouse. The transmission electron micrograph of the same vessel (bottom left) shows an endothelial cell (marked EC), erythrocyte (marked E) and lumen (marked L). The image of a gold grid is derived from the *Electron Microscopy Sciences* website. Permission to use this image was granted.

2.7. ICP-MS

ICP-MS (Agilent 7700x; Agilent Technologies, Santa Clara, CA, USA) was equipped with a conventional Meinhard nebulizer, a Peltier-cooled Scott double-channel spray chamber (temperature 275 K) and a shield torch. The sample introduction system used was nickel sampling and skimmer cones, a CE lens stack, an octopole collision/reaction cell with helium gas (Matheson Gas Products, Parisppany, NJ, USA) (purity of 99.999%), a quadrupole mass analyzer with a dwell time of 200 ms per isotope and an electron multiplier for detection. Instrumental parameters were as follows: forward power, 1500 W; plasma gas flow rate, 15.0 L min^{-1}; auxiliary gas flow rate, 1.0 L min^{-1}; carrier gas flow rate, 0.99 L min^{-1}; make-up gas flow rate, 0.14 L min^{-1}; monitored isotopes, ^{63}Cu, ^{65}Cu, ^{45}Sc. The calibration range was from 0.2 to 25 p.p.b., using scandium as internal standard in a final concentration of 10 p.p.b. A certified water reference material (CRM-TMDW) was applied to verify the accuracy of the analytical method. For testing the effectiveness of the digestions, the dogfish muscle CRM, DORM-3, was analyzed in the same way as the samples. Each analysis was performed twice.

3. Results and discussion

The biological value of chemical sample preparation for biometal study has been well demonstrated by several studies using SRXRF or EDX (Finney *et al.*, 2007; Kehr *et al.*, 2009; Kemner *et al.*, 2004; Fuentealba *et al.*, 1993; Paris-Palacios & Biagianti-Risbourg, 2006). An ideal sample preparation approach for biological metal imaging should prevent exogenous metal introduction and endogenous metal leaching, and maintain the tissue integrity simultaneously. First, we determined the copper concentration in the chemicals used for TEM. Glutaraldehyde (50%) and osmium tetroxide (4%) were diluted five times with Milli-Q water. After using an internal standard (up to 100 p.p.b. of Sc) the samples were analyzed for copper concentration by ICP-MS. The resin (200 mg) was mixed with 500 µl of 30% HNO_3 and the internal standard, and then digested by microwaves for 45 min. The solution was then analyzed for copper concentration by ICP-MS. Our result showed that copper concentrations in osmium tetroxide (4%), glutaraldehyde (2.5%) and resin (200 mg) were not higher than the detection limits. The detection limit for osmium tetroxide and glutaraldehyde is 0.09 ng ml^{-1} and for resin is 1.3 ng g^{-1}. As compared with a representative copper concentration in normal human serum (70–155 µg dl^{-1}, or 700–1550 ng ml^{-1}), the exogenous introduction of copper from these chemicals into biological samples during TEM preparation is negligible. Consistent with our observation, Paris-Palacios & Biagianti-Risbourg (2006) used EDX to scan the empty areas of resin section prepared using the TEM procedure, showing that copper signals are undetectable in TEM embedding media. Second, another major factor that affects the biological copper image is that a small amount of copper is leached from the tissue during sample preparation. Although there is no method for accurately evaluating this loss so far, a recent study showed a good agreement to detect the biometal contents between glutaraldehyde-fixed and unfixed cells, hinting that fixation does not increase biometal leaching from the cells (Twining *et al.*, 2003). Theoretically, free copper in the cell is extremely low (Rae *et al.*, 1999) and copper is believed to be largely bound to proteins that can be tightly fixed by glutaraldehyde. Third, the glutaraldehyde-fixed and resin-embedded approach has been well accepted for pathological research in medicine because of its capacity to preserve the tissue integrity. More important, the relative topography of copper observed in different areas of a cell or tissue section is fairly consistent; the fixation and embedding are processed using a standardized protocol. Thus, glutaraldehyde fixation and resin embedding is a reasonable approach for preparing samples used for the study of the spatial association between copper and cellular structure.

3.1. Optimizing the thickness of THP-1 cell sections for SRXRF

Currently, the typical thickness of the cell or tissue sections for SRXRF is between 4 and 10 µm. The ultramicrotome used for TEM sampling could maintain the cellular structure at as low as 90 nm section thickness. Therefore we examined the minimum thickness in THP-1 cell sections that can be achieved for SRXRF. First, as in our previous study (1 s of dwell time for the whole THP-1 cell monolayer without sectioning) (Kim *et al.*, 2012), with 1.5 s of dwell time, copper can be detected in whole cells up to 10 µm of section thickness. After increasing the dwell time to 4 s, the spatial topography of copper can be measured in 1 µm of section thickness (semithin). However, ultrathin sections (90 nm) cannot provide sufficient signal for copper detection under our experimental conditions. Our further experiment also showed that copper topography can be measured in the 1 µm-thick sections with 4 s of dwell time in the mouse aorta. Therefore, these parameters for specimen thickness (1 µm) and dwell time (4 s) were applied in the following experiments.

It is necessary to note that the specimen thicknesses for TEM and SRXRF likely depend on the nature of the element. For example, Chen *et al.* (2006) measured the cellular topography of platinum in a human melanoma cell line after treatment with a platinum-containing compound. In this study the exogenous platinum and endogenous zinc can be detected at a thickness of 300 nm of the cell line section (Chen *et al.*, 2006).

3.2. Copper topography in THP-1 cells

Human THP-1 cells are widely used as a monocyte and macrophage model cell line (Qin, 2012). Our studies indicate that this cell line is also a reasonable model for studying copper metabolism (Kim *et al.*, 2012; Qin *et al.*, 2010; Afton *et al.*, 2009). In our previous study using the full non-dividing THP-1 cell monolayer without sectioning, and comparing the location of zinc, a substantial amount of copper was observed in the nucleus (Kim *et al.*, 2012). TEM can delineate not only the boundary but also the ultrastructure of the nucleus. For example, under TEM the nucleolus is a dense non-membranous structure within the nucleus (Fig. 2*a*). After overlapping the TEM and SRXRF images, our current study reveals that in a representative non-dividing THP-1 cell copper in the nucleolus [43 pmol cm^{-2}; marked as N1 in Fig. 2(*b*)] is slightly higher than the surrounding areas of the nucleus [29 pmol cm^{-2}; marked as Con2 in Fig. 2(*b*)]. Together with previous reports in rat liver (Fuentealba *et al.*, 1993), our studies indicate that nucleolus is a primary copper storage organelle in the nucleus in mammalian cells under certain conditions. Ribosomal RNA is transcribed and assembled within the nucleolus; little is known as to whether copper is involved in the process.

In our current study, by comparing the copper image generated by SRXRF and corresponding cellular structure generated by TEM, Fig. 2(*a*) also reveals that a significant amount of copper is present in two distinctive structures of the cytoplasms in a representative non-dividing THP-1 cell [white arrows in Fig. 2(*a*)]; one is in a perinuclear area [179 pmol cm^{-2}; marked as PN in Fig. 2(*b*)] and the other is adjacent to the cell membrane [51 pmol cm^{-2}; marked as M in Fig. 2(*b*)]. In a mouse embryonic fibroblast cell line treated with 50 µm $CuCl_2$ for 4 h, the average copper area density of

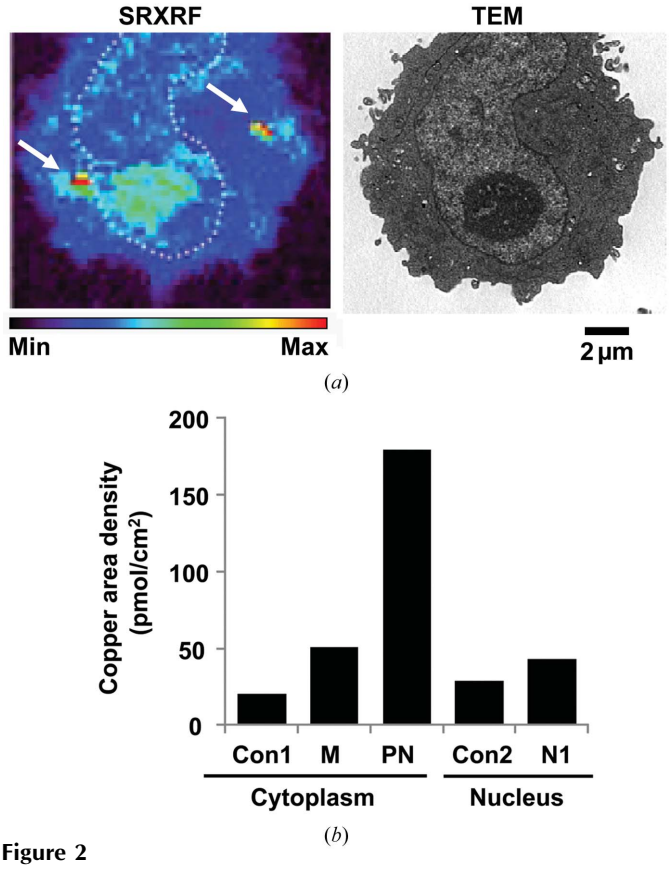

Figure 2
(*a*) Copper location within a human THP-1 cell. A glutaraldehyde-fixed and resin-embedded cell section (1 μm) of human THP-1 cells was mounted on a Gilder finder gold grid to obtain the copper image (left) and cell ultrastructure (right). The location of the nucleus in the copper image was determined by the TEM image (labelled with white dots in the SRXRF image). The colour bar at the bottom left corner represents the relative copper area density, with the dark colour symbolizing a lower area density and grading to red symbolizing an increase in the area density. A black scale bar (2 μm) is shown at the bottom right corner. (*b*) Copper area density in different areas of a THP-1 cell. M and PN represent two higher copper zones in the cytoplasm, plasma membrane area and perinuclear area. An area around the plasma membrane with lowest copper signal was defined as Con1. N1 represents copper in the nucleolus, while Con2 represents the area in the nucleus other than the nucleolus.

cytoplasm is 23 pmol cm^{-2} (McRae *et al.*, 2010). The difference in copper area density between mouse fibroblasts and human THP-1 cells is likely due to the differences in species, copper treatment and sample preparation. In our initial designs we proposed that TEM-SRXRF should clearly detect the copper area density in a specific organelle. This is because the typical size of a nucleus, nucleolus and lysosome is 3–10 μm, 1–3 μm and 0.2–0.5 μm, respectively (Ross & Pawlina, 2011); these organelles are morphologically distinguishable by TEM. However, our experiment demonstrates that, under a comparable resolution with SRXRF, TEM can only detect the nucleus and nucleolus under our conditions; the classic morphology of lysosomes cannot be clearly detected in THP-1 cells. Although the Golgi apparatus can spread the area up to 5–10 μm (Ross & Pawlina, 2011), for our thin cell section the size of the Golgi apparatus is likely to be similar to lysosome. Thus, under a comparable resolution with SRXRF, TEM also did not reveal the classic morphology of Golgi apparatus. However, based on the location, particularly its spatial association with the nucleus and cell membrane as well as previous publications (McRae *et al.*, 2006; Fuentealba *et al.*, 1993), we speculate that the possible structures associated with the copper adjacent to the nucleus and plasma membrane are the Golgi apparatus and lysosomes, respectively.

In Fig. 2 we reported an extensive analysis of copper topography and area density of a representative non-dividing THP-1 cell. In the single-cell-based study it is not surprising that we also observed the single-cell heterogeneity. Specifically, among the non-dividing THP-1 cells that we observed, although we consistently detected a higher copper accumulation in the nucleus and nucleolus, in some single cells we cannot detect significant copper accumulation in cytoplasms, hinting at a more dynamic copper process in cytoplasms. The SRXRF image reflects a snapshot of this process. Thus, the details of single-cell heterogeneity and its impact on copper topography and area density are subjected to further studies.

3.3. Copper topography in the mouse aorta

Copper plays an important role in the formation of elastin and collagen in the aorta. In our previous study we reported that copper, but not zinc, phosphor or sulfur, is accumulated in the elastic laminae of rat aortic media by comparing the cellular structure detected by hematoxylin and eosin staining and Verhoeff's staining (Qin, Toursarkissian *et al.*, 2011). In the current study we first confirmed this finding in another model, in which copper preferentially accumulates in the elastic laminae of murine aortic media (Fig. 3). Moreover, the advantage of TEM is that it can clearly differentiate elastin from collagen in murine aorta (Takaluoma *et al.*, 2007), and helps us to visualize the spatial association between copper and collagen. Fig. 3 shows that the copper level in collagen [16 pmol cm^{-2}; marked as C in Fig. 3(*b*)] is similar to cytoplasms of vascular smooth muscle cells [VSMCs, 14 pmol cm^{-2}; marked as Con in Fig. 3(*b*)] and lower than that in the elastin [40 pmol cm^{-2}; marked as E in Fig. 3(*b*)] and the nucleus of VSMCs [22 pmol cm^{-2}; marked as N2 in Fig. 3(*b*)]. In our previous study using rat aorta, the maximum copper area density is 102 pmol cm^{-2}, which is higher than that in mouse aorta. Although the exact reason for this discrepancy is unknown, the differences in rodent species and sample preparation may play a role. In addition, there are two strong spots in Fig. 3(*a*) around the nucleus of the centre VSMC. So far, we cannot exclude the possibility that these spots are artifacts, because these spots have a sharp contrast with the surroundings and do not occur in other elastic units. Thus, our copper density analysis in Fig. 3(*b*) did not include the signals from these spots. Note also that in Figs. 2(*a*) and 3(*a*) there are some differences in cell and tissue structure between TEM and SRXRF images. These differences are likely due to the following three reasons. First, TEM and SRXRF images are generated by different equipment settings. Second, the tissue and cell sections are processed through different procedures

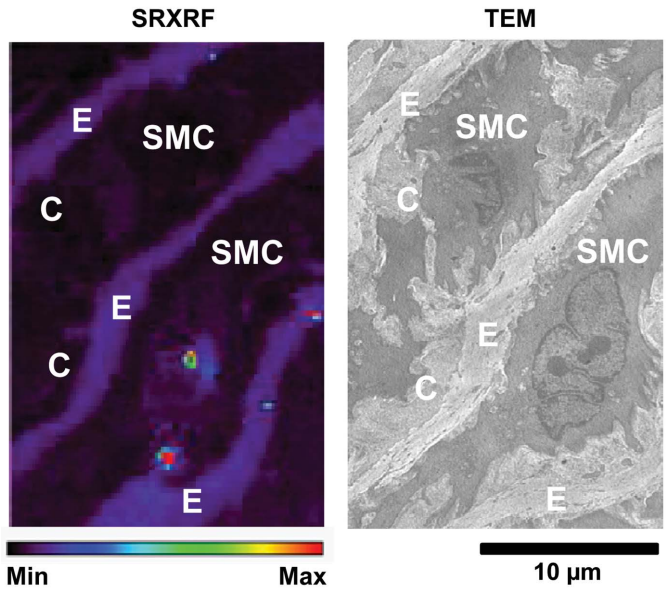

(*a*)

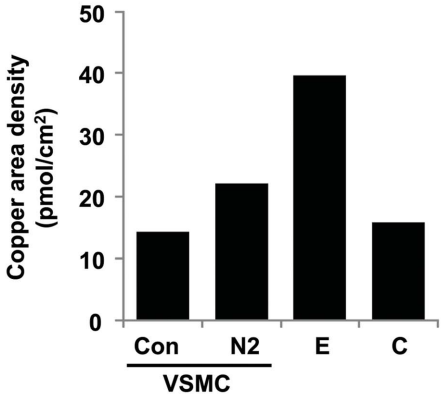

(*b*)

Figure 3
(*a*) Copper location in the aortic media of a C57B/l mouse. A glutaraldehyde-fixed and resin-embedded cell section (1 µm) of a mouse aorta was mounted on a Gilder finder gold grid to obtain the images of copper (left) and tissue ultrastructure (right). The transmission electron micrograph of the aortic media shows vascular smooth muscle cells (marked SMC) and the collagen (marked C) and elastic layers (marked E). The colour bar at the bottom left corner represents the relative copper area density, with the dark colour symbolizing a lower area density and grading to red symbolizing an increase in the area density. A black scale bar (10 µm) is shown at the bottom right corner. (*b*) Copper area density in different areas of a mouse aortic media. The cytoplasm of VSMC is defined as Con. N2 represents a regular nuclear area in VSMC. C and E represent collagen and elastin, respectively.

to meet the requests of TEM and SRXRF. Third, the comparable areas between the TEM and SRXRF images are selected manually. Hopefully an automatic procedure can be introduced in the future to improve the outcome.

Moreover, based on this observation from Fig. 3 that the copper association between elastin and collagen is different, we speculate that the formation of elastin and collagen is processed under different copper concentrations. Indeed, previous study hints that the formations of elastin and collagen may have different sensitivities to dietary copper deficiency. For example, Weissman *et al.* (1963) reported that certain copper-deficient swine only reduce the elastin content, but with no alteration to the collagen content. Furthermore, the extracellular cuproenzyme, lysyl oxidase, plays a key role in catalyzing the cross-linking of collagen and elastin *via* oxidative deamination of lysine or hydroxylysine side chains. Although knockout of the lysyl oxidase expression results in aortic aneurysms in mice, only discontinuous VSMC layers and fragmented elastic laminae were observed in the aneurysmatic aorta using electron microscopy (Mäki *et al.*, 2002; Hornstra *et al.*, 2003). A similar finding was also reported in lysyl oxidase-like 1 protein deficient mice, in which the loss of elastic fibers was observed whereas the abundance and morphology of collagen was not altered compared with control mice (Liu *et al.*, 2004). Thus, it will be intriguing to use TEM-SRXRF to investigate the vascular copper topography in these genetically modified mice.

3.4. Potential application of TEM-SRXRF in cardiovascular disease

Copper metabolism has long been speculated to play a role in the pathogenesis of cardiovascular disease, such as atherosclerosis. For example, human population studies show an association between increased plasma copper levels and atherosclerosis, and elevated copper levels have been detected in human atherosclerotic plaques *versus* healthy controls (Easter *et al.*, 2010). Because the copper is inhomogeneously distributed in tissues and cells, it is highly likely that the participation of copper in the pathogenesis of cardiovascular disease is not only dependent on an alteration of copper concentration but also dependent on a shift of copper topography. Thus, TEM-SRXRF can be used to test this hypothesis using human and animal tissues in the future.

4. Conclusion

In this study, using a glutaraldehyde-fixed and resin-embedded approach, we investigated the correlation between copper topography and subcellular structure in the human THP-1 cell and mouse aortic tissue with 1 µm-thick sections using TEM-SRXRF. Our results indicate that the images generated between TEM and SRXRF are complementary and provide a more accurate image to evaluate the biological copper topography in vascular cells and tissues.

This work was supported by an AHA National Scientist Development Grant (0835268N). Use of the Advanced Photon Source was supported by the US Department of Energy, Office of Science, Office of Basic Energy Sciences, under Contract No. DE-AC02-06CH11357.

References

Abe, A., Yamashita, S. & Noma, A. (1989). *Clin. Chem.* **35**, 552–554.
Afton, S., Caruso, J., Britigan, B. & Qin, Z. (2009). *Biometals*, **22**, 531–539.
Altamura, C., Squitti, R., Pasqualetti, P., Gaudino, C., Palazzo, P., Tibuzzi, F., Lupoi, D., Cortesi, M., Rossini, P. M. & Vernieri, F. (2009). *Stroke J. Cerebr. Circ.* **40**, 1282–1288.
Beauchemin, D. (2002). *Anal. Chem.* **74**, 2873–2894.

Becker, J. S., Niehren, S., Matusch, A., Wu, B., Hsieh, H.-F., Kumbatim, U., Hamester, M., Plaschke-Schlütter, A. & Salber, D. (2010). *Int. J. Mass Spectrom.* **294**, 1–6.
Canatan, H., Bakan, I., Akbulut, M., Halifeoglu, I., Cikim, G., Baydas, G. & Kilic, N. (2004). *Biol. Trace Elem. Res.* **100**, 117–123.
Chen, K. G., Valencia, J. C., Lai, B., Zhang, G., Paterson, J. K., Rouzaud, F., Berens, W., Wincovitch, S. M., Garfield, S. H., Leapman, R. D., Hearing, V. J. & Gottesman, M. M. (2006). *Proc. Natl. Acad. Sci.* **103**, 9903–9907.
Chevallier, P., Dhez, P., Erko, A., Firsov, A., Legrand, F. & Populus, P. (1996). *Nucl. Instrum. Methods Phys. Res. B*, **113**, 122–127.
Dash, P. K., Redell, J. B., Hergenroeder, G., Zhao, J., Clifton, G. L. & Moore, A. (2010). *J. Neurosci. Res.* **88**, 1719–1726.
Easter, R. N., Qilin, C., Lai, B., Ritman, E. L., Caruso, J. A. & Zhenyu, Q. (2010). *Vasc. Med.* **15**, 61–69.
Espen, P. van (2002). *Spectrum Evaluation Handbook of X-ray Spectrometry*, 2nd ed. New York: Marcel Dekker.
Finney, L., Mandava, S., Ursos, L., Zhang, W., Rodi, D., Vogt, S., Legnini, D., Maser, J., Ikpatt, F., Olopade, O. I. & Glesne, D. (2007). *Proc. Natl. Acad. Sci. USA*, **104**, 2247–2252.
Fuentealba, I. C., Davis, R. W., Elmes, M. E., Jasani, B. & Haywood, S. (1993). *Exp. Mol. Pathol.* **59**, 71–84.
Glesne, D., Vogt, S., Maser, J., Legnini, D. & Huberman, E. (2006). *J. Struct. Biol.* **155**, 2–11.
Gross, J. B. Jr., Myers, B. M., Kost, L. J., Kuntz, S. M. & LaRusso, N. F. (1989). *J. Clin. Invest.* **83**, 30–39.
Hornstra, I. K., Birge, S., Starcher, B., Bailey, A. J., Mecham, R. P. & Shapiro, S. D. (2003). *J. Biol. Chem.* **278**, 14387–14393.
Irons, R., Schenk, E. & Giauque, R. (1976). *Clin. Chem.* **22**, 2018–2024.
Jonas, L., Fulda, G., Salameh, T., Schmidt, W., Kroning, G., Hopt, U. T. & Nizze, H. (2001). *Ultrastruct. Pathol.* **25**, 111–118.
Jones, K. W., Gordon, B. M., Hanson, A. L., Kwiatek, W. M. & Pounds, J. G. (1988). *Ultramicroscopy*, **24**, 313–328.
Kehr, S., Malinouski, M., Finney, L., Vogt, S., Labunskyy, V. M., Kasaikina, M. V., Carlson, B. A., Zhou, Y., Hatfield, D. L. & Gladyshev, V. N. (2009). *J. Mol. Biol.* **389**, 808–818.
Kemner, K. M., Kelly, S. D., Lai, B., Maser, J., O'Loughlin, E. J., Sholto-Douglas, D., Cai, Z., Schneegurt, M. A., Kulpa, C. F. Jr & Nealson, K. H. (2004). *Science*, **306**, 686–687.
Kim, H. W., Chan, Q., Afton, S. E., Caruso, J. A., Lai, B., Weintraub, N. L. & Qin, Z. (2012). *Inflammation*, **35**, 167–175.
Lellingsen, D. G., Horn, N. & Aaseth, J. (2007). *Handbook on the Toxicology of Metals*, 3rd ed., edited by G. F. Nordberg, B. A. Fowler and M. Nordberg. New York: Academic Press.
Liu, X., Zhao, Y., Gao, J., Pawlyk, B., Starcher, B., Spencer, J. A., Yanagisawa, H., Zuo, J. & Li, T. (2004). *Nat. Gen.* **36**, 178–182.
L'vov, B. V. (2005). *J. Anal. Chem.* **60**, 382–392.
McRae, R., Lai, B. & Fahrni, C. J. (2010). *J. Biol. Inorg. Chem.* **15**, 99–105.
McRae, R., Lai, B., Vogt, S. & Fahrni, C. J. (2006). *J. Struct. Biol.* **155**, 22–29.
Mäki, J. M., Räsänen, J., Tikkanen, H., Sormunen, R., Mäkikallio, K., Kivirikko, K. I. & Soininen, R. (2002). *Circulation*, **106**, 2503–2509.
Meguid, N. A., Dardir, A. A., El-Sayed, E. M., Ahmed, H. H., Hashish, A. F. & Ezzat, A. (2010). *Clin. Biochem.* **43**, 963–967.
Paris-Palacios, S. & Biagianti-Risbourg, S. (2006). *Aquat. Toxicol.* **77**, 306–313.
Pilloni, L., Lecca, S., Van Eyken, P., Flore, C., Demelia, L., Pilleri, G., Nurchi, A. M., Farci, A. M., Ambu, R., Callea, F. & Faa, G. (1998). *Histopathology*, **33**, 28–33.
Qin, Z. (2012). *Atherosclerosis*, **221**, 2–11.
Qin, Z., Caruso, J. A., Lai, B., Matusch, A. & Becker, J. S. (2011). *Metallomics* **3**, 28–37.
Qin, Z., Konaniah, E. S., Neltner, B., Nemenoff, R. A., Hui, D. Y. & Weintraub, N. L. (2010). *J. Lipid Res.* **51**, 1471–1477.
Qin, Z., Toursarkissian, B. & Lai, B. (2011). *Metallomics*, **3**, 823–828.
Rae, T. D., Schmidt, P. J., Pufahl, R. A., Culotta, V. C. & O'Halloran, T. V. (1999). *Science*, **284**, 805–808.
Ralle, M., Huster, D., Vogt, S., Schirrmeister, W., Burkhead, J. L., Capps, T. R., Gray, L., Lai, B., Maryon, E. & Lutsenko, S. (2010). *J. Biol. Chem.* **285**, 30875–30883.
Ross, M. & Pawlina, W. (2011). Editors. *Histology, A Text and Atlas*, 6th ed. New York: Wolters Kluwer.
Szerdahelyi, P. & Kasa, P. (1984). *Intl. Rev. Cytol.* **89**, 1–33.
Takaluoma, K., Hyry, M., Lantto, J., Sormunen, R., Bank, R. A., Kivirikko, K. I., Myllyharju, J. & Soininen, R. (2007). *J. Biol. Chem.* **282**, 6588–6596.
Taneja, S. K. & Mandal, R. (2007). *Biol. Trace Elem. Res.* **120**, 61–73.
Twining, B. S., Baines, S. B., Fisher, N. S., Maser, J., Vogt, S., Jacobsen, C., Tovar-Sanchez, A. & Sanudo-Wilhelmy, S. A. (2003). *Anal. Chem.* **75**, 3806–3816.
Vogt, S. (2003). *J. Phys. IV Fr.* **104**, 635–638.
Weissman, N., Shields, G. S. & Carnes, W. H. (1963). *J. Biol. Chem.* **238**, 3115–3118.
Yun, W., Lai, B., Cai, Z., Maser, J., Legnini, D., Gluskin, E., Chen, Z., Krasnoperova, A., Valdimirsky, Y., Cerrina, F., Di Fabrizio, E. & Gentili, M. (1999). *Rev. Sci. Instrum.* **70**, 2238–2241.